ADVANCED ELECTRONIC MATERIALS
Open Access
www.advelectronicmat.de

Effect of Molecular Weight on the Morphology of a Polymer Semiconductor–Thermoplastic Elastomer Blend

Amnahir Peña-Alcántara, Shayla Nikzad, Lukas Michalek, Nathaniel Prine, Yunfei Wang, Huaxin Gong, Elisa Ponte, Sebastian Schneider, Yilei Wu, Samuel E. Root, Mingqian He, Jeffrey B.-H. Tok, Xiaodan Gu, and Zhenan Bao**

Polymer semiconductors (PSCs) are essential active materials in mechanically stretchable electronic devices. However, many exhibit low fracture strain due to their rigid chain conformation and the presence of large crystalline domains. Here, a PSC/elastomer blend, poly[(2,6-bis(thiophen-2-yl)-3,7-bis(9-octylnonadecyl)thieno[3,2-b]thieno[2′,3′:4,5]thieno[2,3-d]thiophene)-5,5′-diyl) (2,5-bis(8-octyloctadecyl)-3,6-di(thiophen-2-yl)pyrrolo[3,4-c]pyrrole-1,4-dione)-5,5′-diyl]] (P2TDPP2TFT4) and polystyrene-*block*-poly(ethylene-ran-butylene)-*block*-polystyrene (SEBS) are systematically investigated. Specifically, the effects of molecular weight of both SEBS and P2TDPP2TFT4 on the resulting blend morphology, mechanical, and electrical properties are explored. In addition to commonly used techniques, atomic force microscopy-based nanomechanical images are used to provide additional insights into the blend film morphology. Opposing trends in SEBS-induced aggregation are observed for the different P2TDPP2TFT4 molecular weights upon increasing the SEBS molecular weight from 87 to 276 kDa. Furthermore, these trends are seen in device performance trends for both molecular weights of P2TDPP2TFT4. SEBS molecular weight also has a substantial influence on the mesoscale phase separation. Strain at fracture increases dramatically upon blending, reaching a maximum value of 640% ± 20% in the blended films measured with film-on-water method. These results highlight the importance of molecular weight for electronic devices. In addition, this study provides valuable insights into appropriate polymer selections for stretchable semiconducting thin films that simultaneously possess excellent mechanical and electrical properties.

1. Introduction

Polymer semiconductors (PSCs) are a promising class of materials for creating flexible and stretchable electronic devices, such as organic field-effect transistors (OFETs),[1–4] organic light-emitting diodes,[5–7] and organic solar cells.[8–10] These PSCs are solution-processable, allowing lightweight, large-area, and low-cost electronic devices to be conformable to various surfaces, such as on the human body.[11,12] However, despite the relatively low crystallinity of high-performance PSCs, their rigid molecular structures limit the intrinsic flexibility and stretchability, which suffer from fracture under strain below 10%.[13,14] To date, several methods have been employed to improve PSC mechanical properties, such as: 1) synthesizing stretchable PSCs with new molecular design concepts,[15–19] 2) blending PSCs with an insulating elastic polymer matrix,[16,20–22] 3) employing structural engineering,[23] such as wrinkles, buckling or porous structures, and 4) incorporating small molecule additives.[24–27]

Blending a PSC with an elastomer is an appealing strategy as it is capable of

A. Peña-Alcántara, E. Ponte
Department of Materials Science and Engineering
Stanford University
Stanford, CA 94305, USA

S. Nikzad, L. Michalek, H. Gong, Y. Wu, S. E. Root, J. B.-H. Tok, Z. Bao
Department of Chemical Engineering
Stanford University
Stanford, CA 94305, USA
E-mail: zbao@stanford.edu

The ORCID identification number(s) for the author(s) of this article can be found under https://doi.org/10.1002/aelm.202201055.

DOI: 10.1002/aelm.202201055

N. Prine, Y. Wang, X. Gu
School of Polymer Science and Engineering
The University of Southern Mississippi
Hattiesburg, MS 3940, USA
E-mail: xiaodan.gu@usm.edu

S. Schneider
Department of Chemistry
Stanford University
USA

M. He
Corning Incorporated
Corning, New York, NY 14831, USA

ADVANCED ELECTRONIC MATERIALS
Open Access
www.advelectronicmat.de

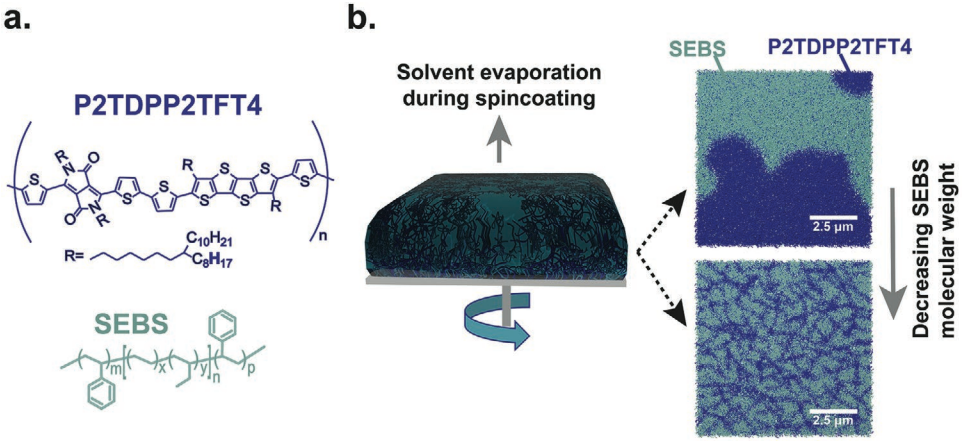

Figure 1. a) Chemical structure of P2TDPP2TFT4 and SEBS. b) Schematic rendering showing solvent evaporation during spin-coating from solution to thin film of the P2TDPP2TFT4/SEBS blends. Two distinctive mesoscale morphologies are represented in a schematic micrograph for the 95k-DPP/82k-SEBS and 95k-DPP/276k-SEBS blends, respectively. P2TDPP2TFT4 is represented by dark blue and SEBS in light blue.

not only improving a film's mechanical properties but also of decreasing the consumption of the costly PSC component and does not require additional synthetic efforts. Moreover, it has been found that with a proper selection of elastic insulating polymer, improved charge transport capabilities of the blend film can be achieved relative to the neat PSC film.[16,20,22] The improved charge-transport property in PSC/elastomer blends has been attributed to optimized film morphologies such as increased PSC backbone planarization and aggregation, more favorable polymer chain alignment along the long axis of nanostructured aggregates, and a well interconnected PSC nanostructure network.[16,20–22] Many previous studies used polystyrene (PS) as the insulating polymer.[28–30] However, recent work showed thermoplastic elastomers can have the added benefits of improving the softness and mechanical robustness of the PSC composite films[20] as PS is typically glassy and has a brittle nature.[31]

Due to the applicability of diketopyrrolopyrrole (DPP)-based PSCs in various fabrication methods,[32,33] we use a DPP-based PSC as our model system, poly[((2,6-bis(thiophen-2-yl)-3,7-bis(9-octylnonadecyl)thieno[3,2-b]thieno[2′,3′:4,5]thieno[2,3-d]thiophene)-5,5′-diyl)(2,5-bis(8-octyloctadecyl)-3,6-di(thiophen-2-yl)pyrrolo[3,4-c]pyrrole-1,4-dione)-5,5′-diyl]] (P2TDPP2TFT4), blended with a thermoplastic elastomer, polystyrene-*block*-poly(ethylene-ran-butylene)-*block*-polystyrene (SEBS). We chose P2TDPP2TFT4 as the PSC because its synthesis has been carefully studied for solution processability and tuning of the molecular weight.[34] DPP-based PSCs are typically semi-crystalline, donor-acceptor type conjugated polymers with a strong tendency for aggregation due to π–π stacking and have been reported to show high charge carrier mobilities in thin film transistor devices.[13,35] Although there has been success in improving electronic and mechanical performance through blending of different elastomers (i.e., polydimethylsiloxane (PDMS) and polyethylene),[16] SEBS was chosen as the insulating elastomer matrix due to its similar surface energy compared to DPP polymers.[20] It was observed previously that DPP-based/ SEBS polymer blends have nanoscale phase-separated morphology of interconnected PSC nanofibrils with reduced conformational defects compared to the neat polymer.[20] A previous study reported that blending another DPP-based PSC, poly-[2,5-bis(7-decylnonadecyl)pyrrolo[3,4-c]pyrrole-1,4-(2 H,5 H)-dione-(E)-(1,2-bis(5-(thiophen-2-yl)selenophen-2-yl)ethene) (DPPDTSE), with SEBS resulted in a 50% higher field effect mobility compared to the neat DPPDTSE.[20] However, a detailed understanding of the effect of SEBS molecular weight is still missing. Specifically, we hypothesize that SEBS molecular weight may affect the phase separation and microstructure of the blended films, and these morphological parameters will affect the resulting thin-film mechanical and charge transport properties.

The polymer blend solution is a ternary system, which experiences phase separation upon spin-coating as the solvent evaporates. In a polymer blend, morphology and phase separation are influenced by various parameters, such as solvent choice,[36] coating conditions,[21,22] polymer concentration,[37] and polymer molecular weight.[22,26,38–40] Phase separation, dominated either by spinodal decomposition or nucleation and growth, occurs due to polymer–polymer immiscibility depending upon the enthalpic and entropic contributions to the free energy of mixing.[16] In addition, substrate surface energy will influence vertical stratification, which has been used to create self-encapsulated films and enables a one-step process in creating the dielectric and active PSC layers.[16]

The effect of PSC molecular weight on the film morphology in P2TDPP2TFT4/SEBS blends with a constant SEBS molecular weight of 125 kDa was previously studied by our group.[22] We found that aggregation-induced molecular ordering in these blend films was strongly correlated to the molecular weight of the semiconducting component. The higher the molecular weight of PSC used to blend with SEBS, the greater the observed ratio of polymer aggregation, resulting in improved charge transport in OFETs.[22] Prompted by this initial preliminary study, in this current work, we systematically investigate the effects of varying SEBS molecular weight in addition to PSC molecular weight, and test their effects on the blend-film morphology, mechanical properties, and OFET performances. Specifically, P2TDPP2TFT4/SEBS blended films (**Figure 1**a,b) with several combinations of molecular weights (**Table 1**) were analyzed using ultraviolet-visible (UV–vis) absorption spectroscopy, grazing incidence X-ray diffraction (GIXD), X-ray photoelectron

Table 1. Molecular weight, dispersity (*Đ*), and styrene content (wt%) of the different polymers.

Polymer	M_n [kDa]	*Đ*	Styrene content [wt%]
95k-DPP	95	2.49	–
48k-DPP	48	1.91	–
276k-SEBS	276	1.17	28
158k-SEBS	158	1.18	32
82k-SEBS	82	1.01	28
18%ps-93k-SEBS	93	1.09	18
42%ps-72k-SEBS	72	1.10	42

spectroscopy (XPS), atomic force microscopy (AFM), AFM-based infrared-spectroscopy (AFM-IR), and optical microscopy (OM). The mechanical properties of the polymer blends were investigated through film-on-water tensile tests and AFM based nanomechanical mapping. The charge transport properties were measured by characterizing the corresponding OFETs. A schematic of the film formation and final morphology for varying molecular weights is shown in Figure 1b. We observed that the molecular weight of SEBS did not significantly affect the solution-phase pre-aggregation of P2TDPP2TFT4 but did cause changes to the amount of P2TDPP2TFT4 aggregation in thin film. AFM images revealed substantial differences in mesoscale morphology, while mechanical tests revealed changes in strain at fracture and modulus for P2TDPP2TFT4 blends depending on the SEBS molecular weight. Last of all, the field-effect mobility trends, as a measure of charge transport in OFETs, should corelate with the aggregation trends based on the molecular weight of SEBS.

2. Results and Discussion

2.1. Morphology

We first investigated the thin film morphology of blends of various P2TDPP2TFT4 and SEBS molecular weights as well as the styrene content in SEBS (Table 1). Chemical structures of P2TDPP2TFT4 and SEBS are shown in Figure 1a. The films were prepared by spin coating a chlorobenzene solution containing P2TDPP2TFT4: SEBS with 3:7 weight ratio (final P2TDPP2TFT4 concentration of 2 mg mL^{-1} in chlorobenzene) on octadecyltrimethoxylsilane (OTS)-modified silicon wafer[41] or optically clean glass substrates. This weight ratio was chosen as it was previously found to be the typical optimal ratio for several PSC/SEBS blends to give both high charge carrier mobilities and good stretchability, given the maximum amount of aggregation and ideal nanofiber structure being present at this ratio.[20–22]

The absorption spectrum measured by UV–vis spectroscopy allows for determination of changes in the aggregation behaviors of the PSC.[42,43] For P2TDPP2TFT4, typically the absorption band from UV–vis exhibits a broad π–π^* transition of the monomer unit at ≈450 nm. The charge transfer absorption band between 600 and 900 nm shows two vibronic peaks, one at higher energy (0–1 transition) and one at lower energy (0–0 transition), which is normally attributed to polymer aggregation.[42,43] A larger (0–0) to (0–1) peak intensity ratio and bathochromic shift is attributed to a higher fraction of aggregated structures. The red shift of the aggregation peak would be related to either planarization or long-range order.[42–44]

As seen from **Figure 2**a, all blended P2TDPP2TFT4/ SEBS solutions used for film deposition exhibited a similar increase in the (0–0):(0–1) ratio as compared to that of the neat solution of P2TDPP2TFT4. However, no significant bathochromic shift was observed in the solution. The changes in (0–0):(0–1) ratio indicates a slight change in the amount of aggregation; however, there is not much of a difference based on the SEBS molecular weight. Consistent with prior reports,[20–22] all our blend films showed an increased (0–0):(0–1) ratio (aggregation ratio) and a bathochromic red shift of the (0–0) transition, ≈8 nm, as compared to the neat film. This increased ratio and bathochromic shift suggest that blending P2TDPP2TFT4 with SEBS led to more aggregation formation, longer range ordered aggregates, and/or backbone planarization.

We observed that the molecular weight of SEBS gave a weak opposing trend for the ratio of (0–0) to (0–1) transition peaks from the absorption profile for the two molecular weights of P2TDPP2TFT4. In the case of 95k-DPP, decreasing the SEBS molecular weight increased the PSC aggregation ratio in blend thin films, which suggested an increase in the amount of aggregation formation (Figure 2b). On the other hand, for the 48k-DPP, decreasing the molecular weight of SEBS resulted in a slight decrease in aggregation ratio (Figure 2b). We hypothesize that the opposing effects of SEBS molecular weight on aggregation are the product of the interplay between the kinetic trapping caused by the fast solidification rates in spin-coating and thermodynamic interactions. Previous studies have indicated that the kinetics of crystallization will influence the final film morphology.[45] In addition, increasing the molecular weight of a polymer delayed the solidification and crystallization rates of film formation.[46,47] The influence of kinetics (solvent evaporation rate, etc.) on the final film have not been studied in detail for this project; however, future studies should further investigate this phenomenon.

The crystalline structure of the thin films was further investigated using GIXD to observe the impact of molecular weight on the polymer crystallinity. As crystalline packing coherence length (L_C) can influence charge transport;[48] here, we estimated L_C using the Scherrer equation (Equation (1)),

$$L_C = \frac{2\pi K}{\Delta_q} \tag{1}$$

where K is a shape factor and Δ_q is the full-width half-maximum of a diffraction peak.[48] A higher L_C is an indication of a longer range order.[49] In this system, L_C of the (200) reflection was observed to increase when P2TDPP2TFT4 was blended with SEBS (**Figure 3**a, **Table 2**; Figure S1, Supporting Information), as previously reported.[22] L_C from the (200) reflection increased by up to 30% from the 95k-DPP neat film to blends, while it increased by up to 60% for the 48k-DPP blends compared to its neat film. The slightly larger increase in (200) L_C for blended 48k-DPP films (≈1.6-fold) as compared to 95k-DPP films (≈1.3-fold) could be caused by the higher tendency for conformational disorder in the higher molecular weight 95k-DPP compared to

ADVANCED ELECTRONIC MATERIALS
Open Access
www.advelectronicmat.de

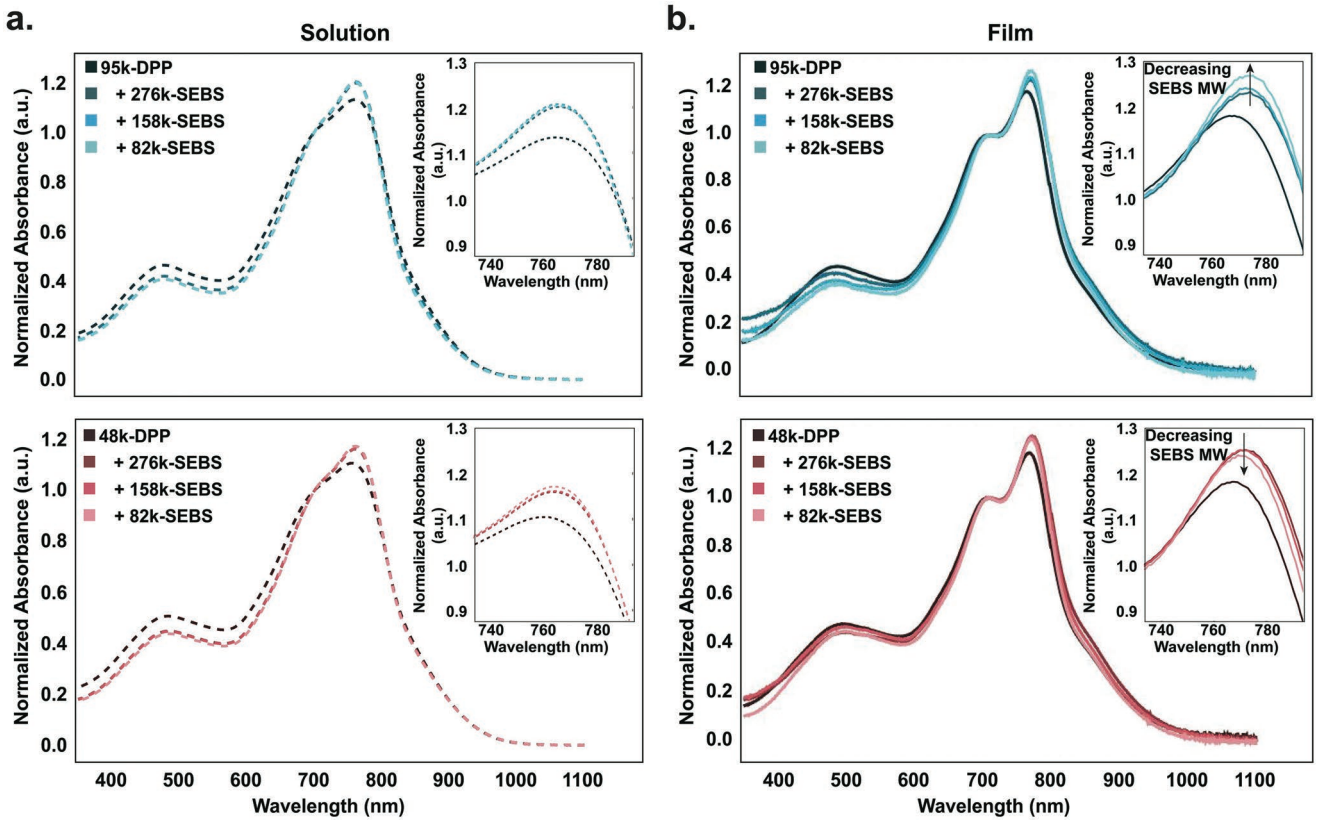

Figure 2. a) Solution UV–vis spectrum of 95k-DPP and 48k-DPP and their blends of variable SEBS molecular weights prepared from solutions with chlorobenzene as the solvent. b) UV–vis spectrum of 95k-DPP and 48k-DPP thin films (chlorobenzene (CB) as the solvent) and their blends of variable SEBS molecular weights annealed at 150 °C for 1 h.

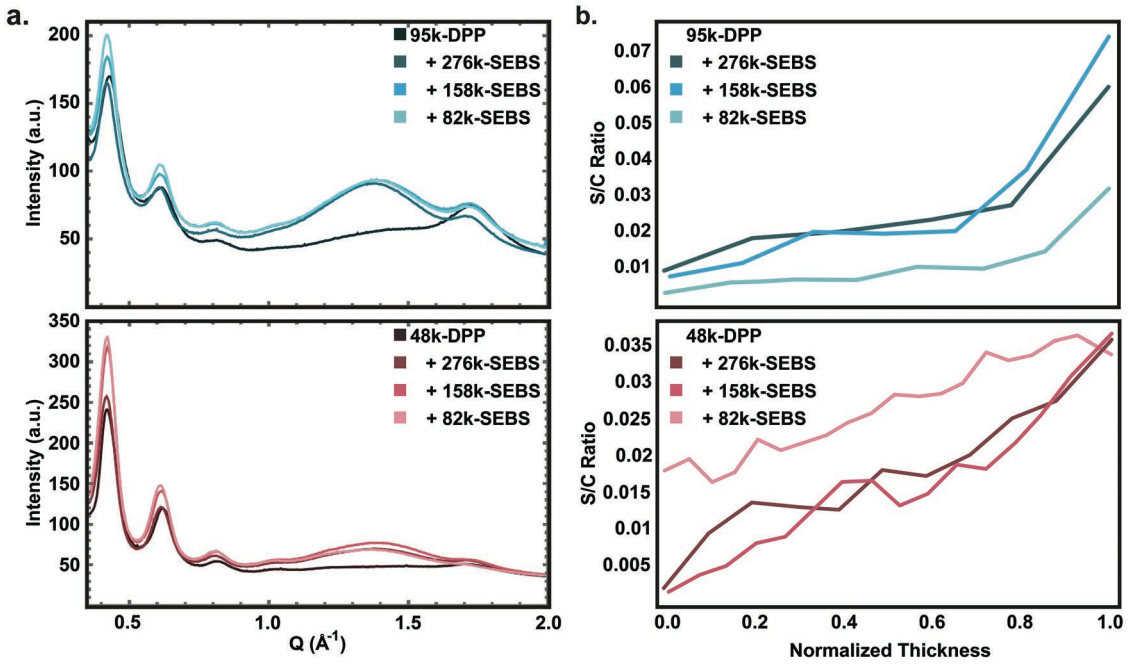

Figure 3. a) 1D GIXD profiles extracted from 2D GIXD patterns for the out-of-plane direction (q_z) of 95k-DPP and 48k-DPP thin film blends of various SEBS molecular weights. b) The ratio of the S 2p to C 1s peak for the 95k-DPP and 48k-DPP polymer blends of different SEBS molecular weights at different depths against their normalized thickness. 1.0 represents the air film interface, while 0 represents the dielectric film interface.

Table 2. Lamellar-spacing, π-stacking distance, and coherence length (L_C) of 95k-DPP and 48k- DPP with their blends with 276k-SEBS, 158k-SEBS, and 82k-SEBS, obtained from GIXD spectrum.

Polymer semiconductor	Elastomer	Lamellar-spacing [Å]	(200) L_C [nm]	π-Stacking [Å]	(010) L_C [nm]
95k-DPP	–	30.2	14.8	3.61	3.27
95k-DPP	276k-SEBS	30.7	19.4	3.63	3.62
95k-DPP	158k-SEBS	30.3	16.3	3.60	4.08
95k-DPP	82k-SEBS	30.6	19.6	3.60	3.37
48k-DPP	–	30.0	16.5	3.68	5.00
48k-DPP	276k-SEBS	30.6	26.1	3.65	5.02
48k-DPP	158k-SEBS	30.4	19.3	3.63	4.46
48k-DPP	82k-SEBS	30.5	22.9	3.66	4.96

the 48k-DPP. On the other hand, the 158k-SEBS gave lower L_c for both molecular weights of P2TDPP2TFT4 compared to the other two SEBS even though this trend was not seen in the UV–vis ratio of the (0–0) and (0–1) transitions. This suggests the blend morphology may be altered by the molecular weight of the SEBS.

The film morphology was further analyzed using a combination of XPS, AFM, AFM-IR, and OM. XPS-based depth profiling was performed to determine the vertical distribution of P2TDPP2TFT4 along the height direction of the blend film. By monitoring the sulfur S(2p) signals (unique to the P2TDPP2TFT4 polymer) and carbon C(1s) signal, we can estimate the Sulphur to Carbon (S/C) ratio; hence, allowing identification as to how P2TDPP2TFT4 was distributed throughout the thickness of the film. Previous SEBS blend studies have found the DPP-based PSC located on both the top and bottom surfaces of the film.[20] However, Tran et al. found that the solubility of a DPP-based PSC impacts the vertical phase separation.[50] Through side-chain engineering, the solubility of the DPP-based PSC is varied. In the case of the more soluble DPP-based PSC, the PSC is concentrated on both the top and bottom surface of the film. On the other hand, with a lower solubility, the DPP-based polymer is found to be concentrated on the top surface.[50] We observed that our blend films have P2TDPP2TFT4 primarily on the air–solid interface (top surface) as opposed to at the semiconductor–dielectric interface (Figure 3b; Figure S2, Supporting Information). There is a gradual change in the concentration of P2TDPP2TFT4 from the air to dielectric interface. The S/C ratio in the thin film at the air interface is 11.8 and 23 times the S/C ratio at the dielectric interface for 95k-DPP and 48k-DPP, respectively (Table S1, Supporting Information). This indicates that the DPP-polymer is concentrated at the top surface of the blend film. This finding is consistent with those published by Tran et al.[50] This is so, given that the molecular weight of P2TDPP2TFT4 (48 and 95 kDa) is large; thus, influencing their solubility and the vertical phase separation.[20]

AFM phase images of both the bottom (**Figure 4**a; Figure S3, Supporting Information) and top (Figure S4, Supporting Information) surfaces of thin films showed island-like structures for P2TDPP2TFT4 when blended with 276k-SEBS that transitioned to uniform nanofibers as SEBS molecular weight decreased to 82k with both 48k-DPP and 95k-DPP. These changes in mesoscale structures can be explained by the changes in miscibility of the polymer blends as well as possibly being influenced by the kinetics of film formation. As molecular weight increases, there is a larger driving force for phase separation due to a smaller entropic gain to the free energy of mixing.[16,40] Indeed, by increasing P2TDPP2TFT4's concentration from 2 to 10 mg mL^{-1} while keeping the weight ratio of P2TDPP2TFT4/SEBS the same (Figure S5, Supporting Information), even in the solution, precipitates were observed in the 95k-DPP/ 276k-SEBS blend, while none were observed in the 95k-DPP/ 82k-SEBS blend. In addition, contact angle measurements (Figure S6 and Table S2, Supporting Information) were conducted to determine the surface energy and estimate the free energy of mixing of the polymer blends. Based on the calculated free energy of mixing (Table S3, Supporting Information), which was dominated by the overall entropy change, increasing the molecular weight of either the P2TDPP2TFT4 or the SEBS increased the driving force for phase separation. The free energy of mixing provides the thermodynamic consideration on the miscibility of the two polymers. However, during film formation, the solution is a ternary system. Future work will be needed on the more complex ternary system.

The SEBS block copolymer microstructure (shown in Figure S7, Supporting Information) also changed in the blended films as its molecular weight varies. SEBS was clearly seen with regularly spaced PS nano-domains surrounding the P2TDPP2TFT4 islands in the 276k-SEBS blends. These PS nano-domains were also visible in the 158k SEBS but became less visible as the SEBS molecular weight decreased to 82k-SEBS. There is a possibility that the SEBS morphology was interrupted due to lower entropic driving force for phase separation with P2TDPP2TFT4 for the lower molecular weight SEBS.

AFM-IR combines AFM with infrared spectroscopy (IR) (FTIR spectra shown in Figure S8, Supporting Information). This experimental tool scans an AFM probe across the sample surface while simultaneously illuminating the area under the probe with a pulsed, tunable infrared laser. When the laser is tuned to the unique infrared absorption bands of the sample, rapid thermal expansion occurs in the material. While in tapping mode, the slight variations in tapping frequency caused by the rapid thermal expansion near the tip are detected as cantilever deflection and can be translated by Fourier transform. Therefore, the technique can distinguish materials in blends by their unique infrared absorption response and map the sample

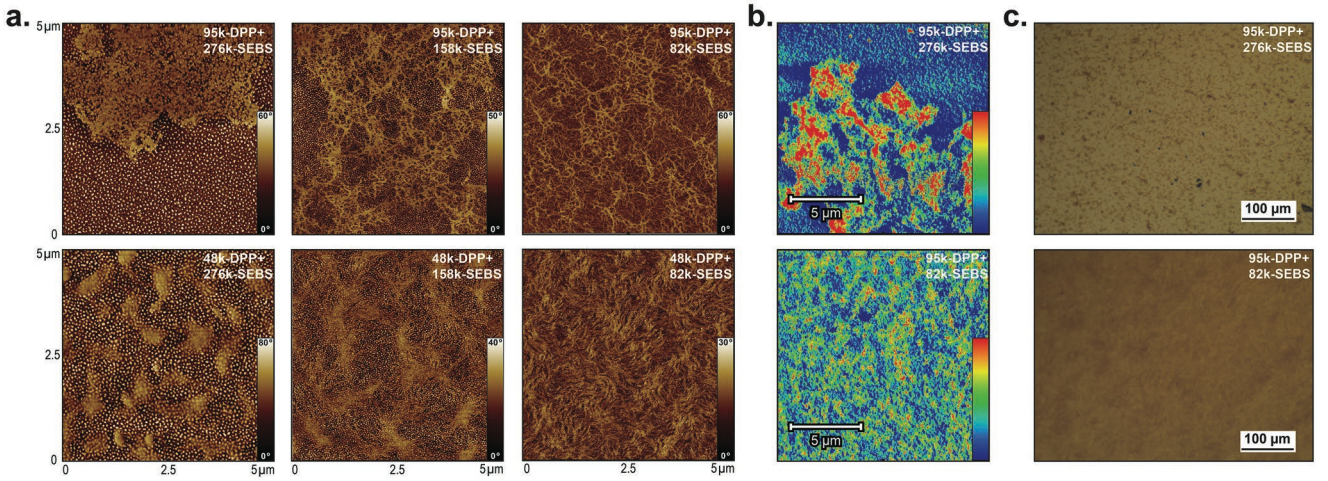

Figure 4. a) Phase AFM images of the bottom surface of 95k-DPP and 48k-DPP polymer blend films with different SEBS molecular weights. b) AFM-IR images of the bottom surface of 95k-DPP blended with 276k-SEBS and 82k-SEBS with an FTIR wavelength of 1659 cm^{-1}. Red regions are those with a larger concentration of DPP while blue regions are those with a lower concentration of DPP. c) OM images of the bottom surface of 95k-DPP blended with 276k-SEBS and 82k-SEBS.

surface as a function of chemical composition.[51] AFM-IR was utilized as a qualitative technique allowing the determination of areas of high concentrations of P2TDPP2TFT4 throughout the film surface. AFM-IR images confirmed that the island-like structures and nanofibers from AFM phase images were regions of higher P2TDPP2TFT4 concentration (Figure 4b; Figures S9 and S10, Supporting Information).

The obtained AFM-IR images further highlighted larger regions of high P2TDPP2TFT4 concentration with increasing P2TDPP2TFT4 and SEBS molecular weights, as seen through the larger clustered green to red regions (5–15 µm in width) of higher concentration of 95k-DPP when blended with 276k-SEBS (Figure 4b; Figure S10, Supporting Information). While in the 95k-DPP and 82k-SEBS blends, there was a more uniform amount of P2TDPP2TFT4 on the surface, seen through the green to red regions. The large islands in 95K-DPP blend films were also visible using OM. Specifically, OM images of 95k-DPP/ 276k-SEBS blended films showed micron-sized domains, which were not present in the smooth films of 95k-DPP/ 82k-SEBS blends (Figure 4c; Figure S11, Supporting Information). We note that despite observing micron-scale P2TDPP2TFT4 enriched domains, our AFM-IR results indicated the presence of a continuous P2TDPP2TFT4 network in 95k-DPP/276k-SEBS films (Figures S7, S9, and S10, Supporting Information).

To investigate whether the observed morphological changes are also dependent on the amounts of PS in SEBS, ≈82 kDa SEBS with different styrene contents was next investigated (Table 1). We observed there was still an increase in the (0–0)/(0–1) ratio and a bathochromic red shift, ≈7 nm, of P2TDPP2TFT4 when blended with this group of various SEBS. However, there was no obvious trend in the (0–0)/(0–1) ratio (Figure S12, Supporting Information), bathochromic shift (Figure S12, Supporting Information), or (200) L_C (Figure S13 and Table S4, Supporting Information) correlated to the styrene content in the SEBS (Figure S12, Supporting Information). AFM phase images (Figures S14 and S15, Supporting Information) and optical images (Figure S16, Supporting Information) were nearly identical regardless of styrene content. Last, P2TDPP2TFT4 was again seen to be primarily concentrated at the air interface rather than the dielectric interface by XPS depth profile (Figure S17, Supporting Information). These results suggest that the molecular weight of SEBS was the dominating factor in impacting P2TDPP2TFT4/SEBS morphology and the PS content in the SEBS played a less significant role. However, we should note that here the effect of styrene content was only studied for ≈82 kDa SEBS. Most SEBS employed in previous studies had a molecular weight of 125 kDa; and thus, the effect of the styrene content at this higher molecular weight may be different.[20–22] We did not use it for our study as there are no commercially available ones with different PS contents for SEBS 125 kDa.

2.2. Mechanical Properties

We next investigated the effect of SEBS molecular weight and the concomitant morphological changes on the film's mechanical properties. The mechanical properties were studied by conducting film-on-water tensile tests and AFM based nanomechanical imaging. Stress–strain curves for the neat and blended films (**Figure 5**a) show large changes in the stress–strain behavior, modulus, and fracture strain. The stress–strain curves of films of the neat P2TDPP2TFT4 (Figure 5a), neat SEBS (Figure S18, Supporting Information), and blends (Figure 5a) show significant differences in stress–strain behavior. Originally, we expected that SEBS would dominate the mechanical properties, given the film composition being majority (70 wt%) SEBS. However, the blend films do not exhibit the pronounced strain stiffening present in neat SEBS (Figure S18, Supporting Information). Thus, the stress–strain behavior is influenced by both the P2TDPP2TFT4 and SEBS. The SEBS has a large influence on the modulus (Figure 5b; Table S5, Supporting Information). The modulus decreases by up to 84% and 75% for 95k-DPP and 48k-DPP, respectively, upon blending. Last of all,

ADVANCED ELECTRONIC MATERIALS
Open Access
www.advelectronicmat.de

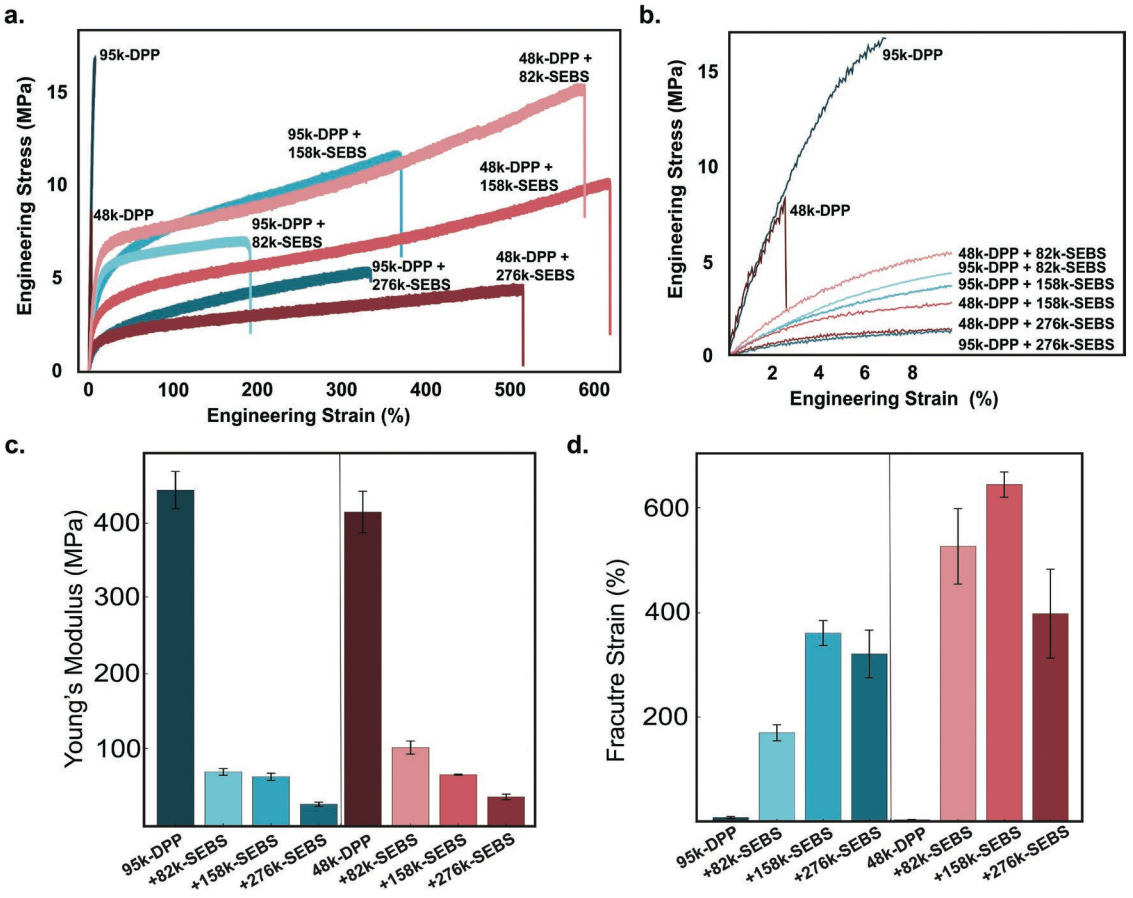

Figure 5. a) Representative stress–strain curves of 95k-DPP and 48k-DPP neat and blended films obtained through film on water tensile tests. b) Zoom in on low strain region of the stress–strain curves of 95k-DPP and 48k-DPP neat and blended films obtained through film on water tensile tests. c) Bar chart showing the Young's modulus of each film. d) Bar chart showing the fracture strain of each film. The error bars represent the standard deviation obtained from three to five different samples.

the fracture strain (Figure 5b; Table S5, Supporting Information) increases by up to 52 and 245 times in the blended films as compared to the neat 95k-DPP and 48k-DPP, respectively.

In terms of the effect of molecular weight, increasing the molecular weight of SEBS decreases the film moduli in both neat SEBS and blend (Table S5, Supporting Information). There are no trends in fracture strain with increasing SEBS molecular weight. However, the fracture strain trends mimic those of the neat SEBS. A complete understanding of the micromechanical failure mechanism and stress–strain behavior is beyond the scope of this paper and should be investigated in future work.

To further investigate the mechanical properties of the blended films, specifically relative to their mesoscale phase separation, AFM based nanomechanical images were collected. For the measurement, a soft cantilever was oscillated through intermittent contact onto the samples surface with a fixed force setpoint to generate force-spectra. With the calibration of the cantilever mechanics and tip radius, the measured force-spectra could be translated into quantitative nanomechanical images, including adhesion, DMT (Derjaguin–Muller–Toporov Model) modulus, deformation (indentation), and dissipation.[52] The nanomechanical property map is in the typical high spatial resolution of an AFM and provides rich information about the blend film, when compared to standard oscillation mode with an amplitude setpoint. In particular, nanomechanical imaging allows for differentiation between properties representing the surface (adhesion and dissipation) and subsurface (modulus and indentation). During the approaching of the cantilever toward the film, if the AFM tip penetrates the sample surface, it would probe the subsurface properties; therefore, providing determination of the DMT modulus and tip indentation depth. However, when the cantilever retracted from the film, the adhesion and dissipation were measured, which were predominantly influenced by the uppermost surface layer.[52]

Nanomechanical images of P2TDPP2TFT4/ SEBS blend films of various P2TDPP2TFT4 molecular weights can be seen in **Figure 6**a (and also in Figures S19 and S20, Supporting Information). The film morphology for all the films is consistent with those imaged in the standard AFM oscillating mode (Figure 4a). However, the modulus and dissipation images provide an increased contrast between P2TDPP2TFT4 and SEBS due to their mechanical differences. Specifically, the P2TDPP2TFT4 regions have a higher modulus (bright green color in modulus map) and lower dissipation (dark blue color in dissipation map) when compared to SEBS regions. Yet, as seen from the oscillating mode AFM images (Figure 4a), the nano-phase

ADVANCED ELECTRONIC MATERIALS
Open Access
www.advelectronicmat.de

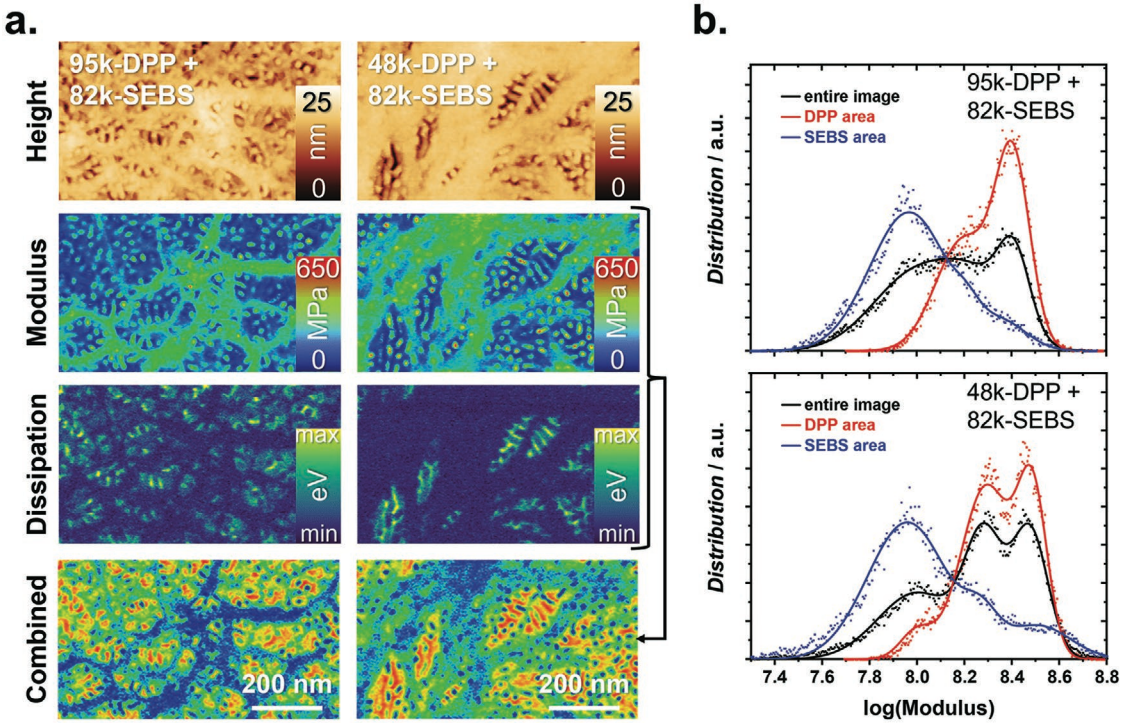

Figure 6. a) Height, DMT modulus, dissipation, and combined (modulus + dissipation) nanomechanical images generated via AFM of the top surface of 95k-DPP/82k-SEBS and 48k-DPP/82k-SEBS. b) Histograms of modulus images (plotted logarithmically) for the entire image (black curves), DPP areas (red curves), and SEBS areas (blue curve).

separation in SEBS can be seen clearly as small dots from the polystyrene domains in Figure 6a (and also in Figures S19 and 20, Supporting Information). In contrast to previous work,[20–22] the SEBS morphology, that is, the dotted features, can even be seen below the P2TDPP2TFT4 regions in the modulus image as it samples the subsurface properties. Specifically, in the 48k-DPP/ 82k-SEBS blend, the SEBS morphology is seen below the P2TDPP2TFT4 fibers in the modulus image but is not visible in the dissipation image. To amplify the difference between the subsurface (modulus) and surface (dissipation) features, the images were arithmetically combined. The resulting images (Figure 6a) displayed contrasting mechanical behaviors for the 95k-DPP/ 82k-SEBS and 48k-DPP/ 82k-SEBS blends. While the 95k-DPP blend showed dark blue fibrous regions, the 48k-DPP blend contained brighter blue and green regions with a visible SEBS morphology. The difference between these two systems indicates that the 95k-DPP/ 82k-SEBS blend consists of relatively thicker P2TDPP2TFT4 fibers on the surface, when compared to the 48k-DPP blend, because no subsurface features of the SEBS morphology could be observed below the fibers of 95k-DPP. To further validate this hypothesis, histograms for the P2TDPP2TFT4 regions, SEBS regions, and the complete image of the modulus images were generated (Figure 6b; Figure S19, Supporting Information). The plotted data for the P2TDPP2TFT4 region (red curves) also indicates a larger contribution of the underlying SEBS morphology (blue curve) for the 48k-DPP blend, which can be explained by a lower thickness of the 48k-DPP fibers on surface when compared to 95k-DPP blends.

Through a similar analysis of the visibility of the SEBS morphology beneath the P2TDPP2TFT4 domains, trends in the relative thickness of PT2DPP2TFT4 regions on the surface of the blended films are also present with variable SEBS molecular weight. In the 95k-DPP blends, as the SEBS molecular weight increases, the surface P2TDPP2TFT4 regions become thinner (Figure 6a; Figure S19a–c, Supporting Information). However, in the 48k-DPP blends, surface P2TDPP2TFT4 regions becomes relatively thicker with increasing SEBS molecular weight (Figure 6a; Figure S19d–f, Supporting Information). A continuous percolation pathway of the PSC is necessary for charge transport. As such, the relative thickness of the P2TDPP2TFT4 regions on the surface (for top contact/bottom gate [TCBG] OFETs) and the connections between these regions will ultimately impact the final device performance. From these experimental results, we hypothesize the relatively thicker top-surface P2TDPP2TFT4 regions will have increased connections with P2TDPP2TFT4 regions deeper within the film; and thus, better device performance.

2.3. FET Characteristics

OFETs were next fabricated to investigate the effect of the characterized morphologies discussed above on the field effect mobility. Both bottom contact/bottom gate (BCBG) (Figure S21, Supporting Information) and TCBG (**Figure 7**) OFET devices were fabricated to account for the possibilities of having vertical gradients of the semiconductor in the film.[53] All output curves are shown in Figure S22, Supporting Information. When compared to previous studies on neat P2TDPP2TFT4 with TCBG devices, our devices had similar mobilities (Figure 7b,c).

ADVANCED ELECTRONIC MATERIALS
Open Access
www.advelectronicmat.de

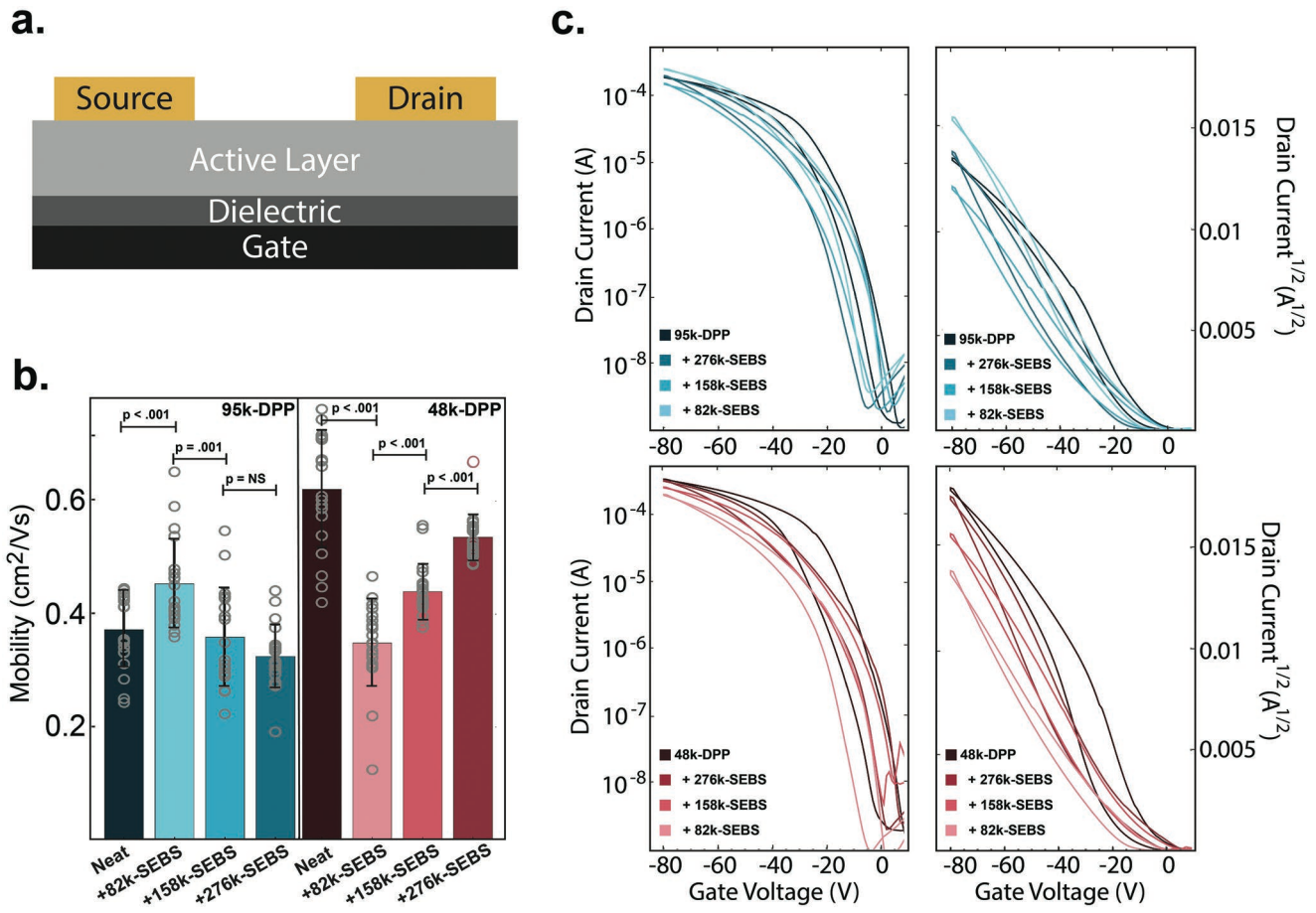

Figure 7. a) Diagram of the top contact/bottom gate OFET. b) Average saturation hole mobility values extracted from OFET. The mobility values obtained for each film are represented by circles. c) Transfer curves of sample OFET for 95k-DPP and 48k-DPP neat and blended films with SEBS of different molecular weights. For each field effect mobility reported, a total of 20 channels on four separate wafers were measured. The source-to-drain voltage was set to −60 V.

Specifically, the previously reported mobility values of 97 kDa P2TDPP2TFT4, extracted from the entire gate voltage regime, were ≈0.35 cm^2 Vs^{-1}, which was comparable to our obtained value of 0.37 cm^2 Vs^{-1}.[34] A mobility value of ≈0.76 cm^2 Vs^{-1} was shown for ≈50 kDa P2TDPP2TFT4, a value close to our 0.62 cm^2 Vs^{-1} for 48 kDa.

Devices fabricated in the BCBG configuration had lower mobilities for both neat and blend films than the corresponding TCBG devices. However, the BCBG devices still showed almost a threefold increase in mobility for blend films as compared to their neat counterpart (Figure S21 and Tables S6 and S7, Supporting Information), indicating there was still an improvement in charge transport in the blend films compared to the neat P2TDPP2TFT4 films, consistent with other previous reports.[20–22] However, given the higher concentration of P2TDPP2TFT4 on the top surface from earlier characterization results, we focused our analysis on TCBG devices. In addition, TCBG devices typically benefit from improved charge injection due to a larger contact area from the source and drain electrodes as compared to the BCBG devices.[54]

In the TCBG devices, only the 95k-DPP/82k-SEBS blended film shows improved charge carrier mobilities as compared to its neat P2TDPP2TFT4 counterpart (Figure 7b,c and **Table 3**). The blend film has a mobility 25% larger than the neat 95k-DPP. All the other blends have comparable or lower mobilities than their neat counterpart (up to 1.74 times lower for the blended film compared to neat). Previous literature reported that blending with a different type of SEBS (125 kDa SEBS with 12 wt PS) resulted in an increase in charge carrier mobility in BCBG device structures, similar to our observed trend.[20,22]

Table 3. Average mobility (μ), on/off current ratio, and threshold voltage of 95k-DPP and 48k-DPP with their blends with 276k-SEBS, 158k-SEBS, and 82k-SEBS, obtained from TCBG devices.

Polymer Semiconductor	Elastomer	μ [cm^2 Vs^{-1}]	On/off current ratio	Threshold voltage [V]
95k-DPP	–	0.37 ± 0.06	10^5	−0.048 ± 5
95k-DPP	276k-SEBS	0.32 ± 0.06	10^4	−1.4 ± 5
95k-DPP	158k-SEBS	0.36 ± 0.09	10^4	0.63 ± 6
95k-DPP	82k-SEBS	0.45 ± 0.08	10^4	0.77 ± 5
48k-DPP	–	0.62 ± 0.1	10^5	−0.44 ± 7
48k-DPP	276k-SEBS	0.54 ± 0.04	10^5	−2.6 ± 5
48k-DPP	158k-SEBS	0.44 ± 0.05	10^5	−3.3 ± 5
48k-DPP	82k-SEBS	0.35 ± 0.08	10^4	−4.5 ± 4

We hypothesized that the lack of improved charge transport in TCBG devices can be explained by the vertical phase separation in the blended films (Figure 3b). Due to the staggered structure of TCBG devices, the charge injection occurs at the top surface (air interface) with the channel still present at the bottom surface (dielectric interface); thus, the charge must travel through the entire film thickness.[54] As such, the vertical phase separation will ultimately affect charge transport throughout the depth of the film. The AFM based nanomechanical imaging results (Figure 7c,d) highlight the difference in thickness and connectivity of the P2TDPP2TFT4 islands/fibers on the surface, which could affect the charge injection and mobility through TCBG devices. The difference in P2TDPP2TFT4 island/fiber thickness is consistent with the 95k-DPP/ 82k-SEBS blends having larger mobility values than the 48k-DPP/ 82k-SEBS blends, given the thin formation and worse continuity of 48k-DPP fibers on the top surface as opposed to the thicker 95k-DPP fibers, suggesting the differences in SEBS impact the device performance. A schematic of the charge transport is shown in **Figure 8**a,b, highlighting the influence vertical phase separation has on the device performance.

Moreover, the mobility trends mimic the trends in the ratio of the (0–0) and (0–1) transition seen by UV–vis, suggesting the small changes in P2TDPP2TFT4 aggregation affected by the addition of various SEBS molecular weights sensitively impact the thin film charge transport. Although the field effect mobility change is small, almost all (except for the difference between 95k-DPP/158k-SEBS and 95k-DPP/276k-SEBS blends) of the trends are statistically significant with a *p*-value less than 0.01. In addition, given the importance in the film formation conditions on final thin film morphology, future work should focus on understanding the kinetics of solvent evaporation and film solidification during film formation.

Last, devices were fabricated from blends with SEBS of various styrene content while keeping the molecular weight of the SEBS comparable. In TCBG devices, it was observed that films with decreasing styrene content had increased mobilities regardless of P2TDPP2TFT4 molecular weight (Figures S23 and S24 and Table S8, Supporting Information), with the highest mobility obtained with 18 wt% styrene content. Even though the origin of this trend is not clearly understood, this observation is consistent with previous literatures that have typically used SEBS with a styrene content of 12 wt% and observed improved charge transport capabilities within blended films of different styrene contents.[20–22]

3. Conclusion

A detailed and systematic study on the effects of polymer molecular weight on the morphology, mechanical behavior, and transistor performance of P2TDPP2TFT4/ SEBS blends was conducted. The influence of SEBS and P2TDPP2TFT4 molecular weight on the final film morphology, mechanical properties, and electronic properties can be summarized as follows: 1) Through UV–vis spectroscopy, we observed that the aggregation and planarization of the higher-MW P2TDPP2TFT4 (95k-DPP) slightly decreased upon increasing the SEBS molecular weight (from 82 to 158 and 276 kDa), while an oppositing trend was observed for the lower molecular weight P2TDPP2TFT4 (48k-DPP). 2) AFM and AFM-IR images showed that both high and low molecular-weight P2TDPP2TFT4 formed fibrillar networks in blends with the low-MW SEBS (82 kDa) blend. Both types of P2TDPP2TFT4 exhibited larger island-like domains with the high-MW SEBS (295 kDa). This is due to a larger driving force for phase separation for the higher molecular weight SEBS associated to less entropic gain in the free energy of mixing. 3) The modulus decreased and fracture strain increased upon blending. Compared to the corresponding neat P2TDPP2TFT4 polymer, our blended films reached a fracture strain greater than 600%. 4) The AFM based nanomechanical imaging determined relative surface thickness of the P2TDPP2TFT4 fibers or islands in 95k-DPP versus 48k-DPP blends had opposing trends with increasing SEBS molecular weight. 95k-DPP blends had increasing thickness as SEBS molecular weight decreased, while the opposite was true for 48k-DPP blends. 5) Despite differences in large-scale phase separation, we also observed that device performances matched well with their corresponding aggregation trends. Previous work studied the molecular weight of the DPP-based polymer and found a large influence on final film morphology and device performance. Our results here add information on the effect of the molecular weight of the elastomers on the final blend film morphology and properties. This work shows that molecular weight and composition of the elastomer can be utilized to finely control and optimize the mechanical and

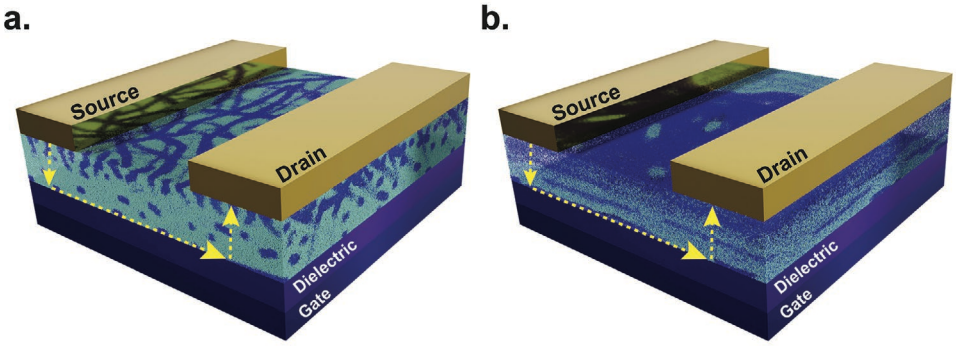

Figure 8. Schematic of the TCBG devices fabricated with a) 82k-SEBS and b) 276k-SEBS. P2TDPP2TFT4 is represented by dark blue and SEBS in light blue. The charge transport pathway is shown through the yellow dashed arrows.

electrical properties of PSC/insulating-polymer blends. These understandings will aid in further improving PSC/elastomer blends for flexible and wearable electronics. Based on the results in this study, future work is still needed on understanding the kinetic process of film formation on PSC/elastomer blends.

4. Experimental Section

Materials: P2TDPP2TFT4 was provided from Corning, Inc. The synthesis for these polymers was reported by Niu et. al.[34] SEBS of variable molecular weights and styrene content (G1633: 276 kDa, G1654: 158 kDa, 1652: 82k Da) and a styrene content 30 wt% were purchased from Kraton, Inc. SEBS of variable styrene content was purchased from Asahi Kasei (Tuftec H1062: 18 wt% St, H1051: 42 wt% St). Gel permeation chromatography of all of the polymers is shown in Figures S25–S30, Supporting Information.

Thin Film Preparation: P2TDPP2TFT4 solution was prepared by dissolving 3 mg in 1 mL of CB, which was heated overnight at 100 °C. Previous studies focused on blended solutions with a final P2TDPP2TFT4 concentration of 3 mg mL^{-1} in CB.[20–22] However, because the 95k-DPP formed precipitates when blended with the 276k-SEBS at the previously used concentration (Figure S1, Supporting Information), in this study, a lower concentration was used. In addition, the SEBS used for this study had a higher styrene content (≈30 wt%) than those previously studied (≈12 wt%)[20–22] because commercially available SEBS of different molecular weights were available only with a higher styrene content. 14.1 mg mL^{-1} solutions of SEBS were created in CB at room temperature and then filtered through a 0.2 µm PTFE filter. Blended solutions were created by mixing 0.66 mL of P2TDPP2TFT4 solution with 0.33 mL of SEBS solution to create 2 mg mL^{-1} DPP solutions with 3:7 weight ratio of P2TDPP2TFT4 : SEBS. Neat and blended solutions were then spin-cast onto OTS-modified[41] silicon wafer (1.5 cm × 1.5 cm). Spin coating was conducted in an N_2-filled glovebox at 1000 rpm for 1 min. The film samples were then annealed at 150 °C for 1 h and slowly cooled to room temperature.

Morphology Characterization: UV–vis spectroscopy was conducted on thin films spin-cast on glass slides using an Agilent Cary 6000i UV/vis/NIR spectrometer. X-ray diffractograms (GIXD) were collected from thin films spin-cast on OTS modified Si wafers at beamline 11-3 in the Stanford Synchrotron Radiation Light Source (SSRL) with a beam energy of 12.7 keV. All the measurements were collected in a helium-purged environment with an X-ray incident angle of 0.12°. AFM images were collected in tapping mode from the Veeco Multimode with a drive frequency of ≈300 kHz and a Tap300Al tip from BudgetSensors (Bulgaria). The bottom sample was measured by using a PDMS stamp to transfer the film. Optical imaging was collected from a Leica DM4000 M light-emitting diode microscope. XPS spectrum was collected from samples spincast on OTS-modified Si wafer using a PHI VersaProbe 3. XPS depth profile was achieved by gas cluster ion beam (GCIB) sputtering with a power of 5 kV 20 nA. Spin cast films were measured using a nanoIR3 AFM-IR from Bruker Instruments (USA) coupled to a MIRcat-QT quantum cascade, mid-infrared laser (frequency range of 917–1700 cm^{-1} and 1900–2230 cm^{-1} using a range of pulse frequencies between 355 and 1382 kHz). AFM-IR data were collected in tapping mode using a gold-coated AFM probe (spring constant [k]: 40 N m^{-1} and resonant frequency [f_o]: 300 kHz) sourced from Bruker. The pulsed mid-IR laser was tuned to frequencies unique to each component as determined by FTIR characterization. Acquired images were flattened using Analysis Studio software.

Mechanical Properties Characterization: For film-on-water tensile tests, Si wafers were initially spincoated with a water soluble poly(sodium 4-styrenesulfonate) (PSS) layer. After that, the neat and blended films were spuncast onto the PSS layer at 1000 rpm for 1 min before being annealed at 150 °C for 1 h and slowly cooled to room temperature. The thickness of the films was measured with an interferometer (Filmetrics Inc. UVX). A oxygen plasma etcher (Diener electronics Inc.) was used to etch the films into a dog-bone shape, and they were then dipped in a water bath to float the dog-bone shaped neat or blended film. The films were then bonded to two aluminum tensile grips coated with a thin layer of PDMS. A high-resolution load cell (KYOWA Inc.) then monitored the force exerted on the film while various strains were applied through a motorized linear stage with a digital encoder (Micronix Inc.). Stress–strain curves were calculated from the force-displacement curves. The stress is equivalent to the force divided by the cross-section area of the dog-bone shaped thin film. The strain is calculated by the displacement in the sample length divided by the original length of the film. Free-standing tensile tests were conducted on Instron 5565.

Nanomechanical imaging was performed on a Bruker Dimension Icon atomic force microscope. NSC19/Al-BS cantilevers were calibrated and used for the measurements. The cantilevers (Estonia) have a nominal resonant frequency of 60 kHz, force constant of 0.5 N m^{-1} and tip radius of 8 nm. The force constant was calibrated by thermal tuning (k = 1.09 N m^{-1}). The deflection sensitivity and tip radius were calibrated on sapphire and Ti reference samples, resulting in a tip radius of 4.1 nm (Bruker-Nanoscope Software – Tip qualification). Force modulation measurements were conducted at a setpoint of 600 pN, peak force frequency of 2 kHz, and an amplitude of 150 nm. The scan resolution and scan rate were set to 256 × 256 pixels and 0.7 Hz. The data were analyzed and depicted with Gwyddion SPM software. The histograms were generated in Gwyddion with a 1D statistical function of masked images.

Contact angle images were taken with a Prosilica GC camera and analyzed using a First Ten Angstroms (FTA32) goniometer. Surface energy was calculated using the Owens–Wendt method:[55]

$$\gamma_s = \gamma_s^p + \gamma_s^d \tag{2}$$

$$(1+\cos\theta_l)\,\gamma_l = 2\left(\sqrt{\gamma_l^d \gamma_s^d} + \sqrt{\gamma_l^p \gamma_s^p}\right) \tag{3}$$

γ_s, γ_s^d, and γ_s^p are the total surface energy, dispersive, and polar component of surface energy of the film, respectively. γ_l, γ_l^d, and γ_l^p are the total surface energy, dispersive, and polar component of surface energy of the test liquid, respectively. For the test liquids used, γ_{water} = 72.8 mJ m^{-2}, γ_{water}^d = 21.8 mJ m^{-2}, γ_{water}^p = 51 mJ m^{-2}, $\gamma_{diiodomethane}$ = 50.8 mJ m^{-2}, $\gamma_{diiodomethane}^d$= 50.8 mJ m^{-2}, and $\gamma_{diiodomethane}^p$ = 0 mJ m^{-2}. The solubility parameter was calculated from:

$$\delta = K\sqrt{\gamma_s} \tag{4}$$

where K is the proportionality constant (K = 116 × 10^3 $m^{-1/2}$).[56] The Flory–Huggins interaction parameter (χ) was estimated with the following equation:[56,57]

$$\chi_{ij} = \frac{V_0}{RT}\left(\delta_i - \delta_j\right)^2 \tag{5}$$

where χ_{ij} is the Flory–Huggins interaction parameter between polymers i and j, V_0 is the geometric mean of the polymer segment molar volume, R is the gas constant, T is the temperature, and δ is the solubility parameter for each polymer. To calculate V_0, the density of P2TDPP2TFT4 was estimated to be 1.05 g cm^{-3}, assuming a similar density to other DPP polymers.[47] The free energy of mixing (ΔG_m) was calculated from the following equation:[58]

$$\Phi G_m = RT\left(\frac{\Phi_i}{N_i}\ln\Phi_i + \frac{1-\Phi_i}{N_j}\ln(1-\Phi_i) + \chi_{ij}\Phi_i(1-\Phi_i)\right) \tag{6}$$

where Φ is the volume fraction and N is the degree of polymerization.

OFET Fabrication and Characterization: For bottom contact/bottom gate devices, Cr/Au (3 nm/40 nm thicknesses) electrodes (width: 4000 µm, length: 200 µm) were evaporated onto the OTS modified SiO_2 wafers. To decrease the contact resistance between the electrodes and the active layer, the electrodes were modified with pentafluorothiophenol.[59] The active layer was then spin-cast onto the electrodes with specifications listed in thin film preparation. For top contact/bottom gate devices, the active layer was spincast on OTS

modified SiO_2 wafers with specifications listed in thin film preparations. MoO_x/Au (3 nm/40 nm thicknesses) electrodes (width: 1000 µm, length: 50 µm) were directly evaporated onto the active layer. OFET transfer and output curves were taken in an N_2-filled glovebox with a Keithley 4200-SCS. Mobility values are average values taken from 8–12 devices. Sample slopes used for the calculation of mobility from the transfer curves are shown in Figure S31, Supporting Information. The source-to-drain voltage was −60 V for all devices. Saturation mobility values (μ) were calculated with the following equation:

$$\mu = \frac{2L}{WC}\frac{\delta\sqrt{I_D}}{\delta V_G} \quad (7)$$

L is the channel length (50 µm), W is the channel width (1000 µm), and C is the gate-channel capacitance per unit area (300 nm SiO_2 dielectric layer) (10.9 nF cm^{-2}). P-values for the field-effect mobilities were calculated using a Student's t-test.

Supporting Information

Supporting Information is available from the Wiley Online Library or from the author.

Acknowledgements

A.P.A. acknowledges support from the National Science Foundation Graduate Research Fellowship Program under Grant No. DGE-1656518 as well as the Stanford Knight–Hennessy Scholarship and the Stanford Enhancing Diversity in Graduate Education Doctoral Fellowship. N.P. and X.G. are thankful for the financial support from NSF (DMR-2047689) for enabling the morphology characterization of stretchable films. L.M. gratefully acknowledges funding through the Walter Benjamin Fellowship Program by the Deutsche Forschungsgemeinschaft (DFG 456522816). The GIXD measurements were made at beamlines 11-3 of the Stanford Synchrotron Radiation Light Source, which are supported by the Director, Office of Science, Office of Basic Energy Sciences, of the US Department of Energy (DE-AC02-76SF00515). Part of this work was performed at the Stanford Nano Shared Facilities (SNSF), supported by the National Science Foundation under award ECCS-2026822. Any opinion, findings, and conclusions or recommendations expressed in this material are those of the authors(s) and do not necessarily reflect the views of the National Science Foundation. This work is supported by US Department of Energy, Office Basic Energy Sciences, Division of Material Science and Engineering, Program on Physical Behaviors of Materials (DE-SC0016523).

Conflict of Interest

The authors declare no conflict of interest.

Data Availability Statement

The data that support the findings of this study are available from the corresponding author upon reasonable request.

Keywords

elastomer, organic field effect transistors, polymer blend, polymer semiconductors

Received: September 29, 2022
Revised: November 19, 2022
Published online:

[1] A. A. Virkar, S. Mannsfeld, Z. Bao, N. Stingelin, *Adv. Mater.* **2010**, *22*, 3857.
[2] M. Chang, G. T. Lim, B. Park, E. Reichmanis, *Polymers* **2017**, *9*, 212.
[3] J. C. Yang, J. Mun, S. Y. Kwon, S. Park, Z. Bao, S. Park, *Adv. Mater.* **2019**, *31*, 1904765.
[4] A. C. Arias, J. D. MacKenzie, I. McCulloch, J. Rivnay, A. Salleo, *Chem. Rev.* **2010**, *110*, 3.
[5] H. Yin, Y. Zhu, K. Youssef, Z. Yu, Q. Pei, *Adv. Mater.* **2022**, *34*, 2106184.
[6] A. Salehi, X. Fu, D.-H. Shin, F. So, *Adv. Funct. Mater.* **2019**, *29*, 1808803.
[7] N. Sun, C. Jiang, Q. Li, D. Tan, S. Bi, J. Song, *J. Mater. Sci.: Mater. Electron.* **2020**, *31*, 20688.
[8] H. Yin, C. Yan, H. Hu, J. K. W. Ho, X. Zhan, G. Li, S. K. So, *Mater. Sci. Eng., R* **2020**, *140*, 100542.
[9] R. Xue, J. Zhang, Y. Li, Y. Li, *Small* **2018**, *14*, 1801793.
[10] G. Wang, F. S. Melkonyan, A. Facchetti, T. J. Marks, *Angew. Chem., Int. Ed.* **2019**, *58*, 4129.
[11] S. Lai, A. Zucca, P. Cosseddu, F. Greco, V. Mattoli, A. Bonfiglio, *Org. Electron.* **2017**, *46*, 60.
[12] S. Wang, J. Xu, W. Wang, G.-J. N. Wang, R. Rastak, F. Molina-Lopez, J. W. Chung, S. Niu, V. R. Feig, J. Lopez, T. Lei, S.-K. Kwon, Y. Kim, A. M. Foudeh, A. Ehrlich, A. Gasperini, Y. Yun, B. Murmann, J. B.-H. Tok, Z. Bao, *Nature* **2018**, *555*, 83.
[13] C. B. Nielsen, M. Turbiez, I. McCulloch, *Adv. Mater.* **2013**, *25*, 1859.
[14] Y. Zheng, S. Zhang, J. B.-H. Tok, Z. Bao, *J. Am. Chem. Soc.* **2022**, *144*, 4699.
[15] G.-J. N. Wang, L. Shaw, J. Xu, T. Kurosawa, B. C. Schroeder, J. Y. Oh, S. J. Benight, Z. Bao, *Adv. Funct. Mater.* **2016**, *26*, 7254.
[16] B. Kang, F. Ge, L. Qiu, K. Cho, *Adv. Electron. Mater.* **2017**, *3*, 1600240.
[17] J. Mun, Y. Ochiai, W. Wang, Y. Zheng, Y.-Q. Zheng, H.-C. Wu, N. Matsuhisa, T. Higashihara, J. B.-H. Tok, Y. Yun, Z. Bao, *Nat. Commun.* **2021**, *12*, 3572.
[18] D. Liu, J. Mun, G. Chen, N. J. Schuster, W. Wang, Y. Zheng, S. Nikzad, J.-C. Lai, Y. Wu, D. Zhong, Y. Lin, Y. Lei, Y. Chen, S. Gam, J. W. Chung, Y. Yun, J. B.-H. Tok, Z. Bao, *J. Am. Chem. Soc.* **2021**, *143*, 11679.
[19] J. Y. Oh, S. Rondeau-Gagné, Y.-C. Chiu, A. Chortos, F. Lissel, G.-J. N. Wang, B. C. Schroeder, T. Kurosawa, J. Lopez, T. Katsumata, J. Xu, C. Zhu, X. Gu, W.-G. Bae, Y. Kim, L. Jin, J. W. Chung, J. B.-H. Tok, Z. Bao, *Nature* **2016**, *539*, 411.
[20] J. Xu, S. Wang, G.-J. N. Wang, C. Zhu, S. Luo, L. Jin, X. Gu, S. Chen, V. R. Feig, J. W. F. To, S. Rondeau-Gagn´e, J. Park, B. C. Schroeder, C. Lu, J. Y. Oh, Y. Wang, Y.-H. Kim, H. Yan, R. Sinclair, D. Zhou, G. Xue, B. Murmann, C. Linder, W. Cai, J. B.-H. Tok, J. W. Chung, Z. Bao, *Science* **2017**, *355*, 59.
[21] J. Xu, H.-C. Wu, C. Zhu, A. Ehrlich, L. Shaw, M. Nikolka, S. Wang, F. Molina-Lopez, X. Gu, S. Luo, D. Zhou, Y.-H. Kim, G.-J. N. Wang, K. Gu, V. R. Feig, S. Chen, Y. Kim, T. Katsumata, Y.-Q. Zheng, H. Yan, J. W. Chung, J. Lopez, B. Murmann, Z. Bao, *Nat. Mater.* **2019**, *18*, 594.
[22] S. Nikzad, H.-C. Wu, J. Kim, C. M. Mahoney, J. R. Matthews, W. Niu, Y. Li, H. Wang, W.-C. Chen, M. F. Toney, M. He, Z. Bao, *Chem. Mater.* **2020**, *32*, 897.
[23] M. Kaltenbrunner, M. S. White, E. D. Głowacki, T. Sekitani, T. Someya, N. S. Sariciftci, S. Bauer, *Nat. Commun.* **2012**, *3*, 770.
[24] J. Mun, J. Kang, Y. Zheng, S. Luo, Y. Wu, H. Gong, J.-C. Lai, H.-C. Wu, G. Xue, J. B.-H. Tok, Z. Bao, *Adv. Electron. Mater.* **2020**, *6*, 2000251.
[25] J. Mun, J. Kang, Y. Zheng, S. Luo, H.-C. Wu, N. Matsuhisa, J. Xu, G.-J. N. Wang, Y. Yun, G. Xue, J. B.-H. Tok, Z. Bao, *Adv. Mater.* **2019**, *31*, 1903912.
[26] J. Xu, H.-C. Wu, J. Mun, R. Ning, W. Wang, G.-J. N. Wang, S. Nikzad, H. Yan, X. Gu, S. Luo, D. Zhou, J. B.-H. Tok, Z. Bao, *Adv. Mater.* **2022**, *34*, 2104747.

[27] M. Nikolka, I. Nasrallah, B. Rose, M. K. Ravva, K. Broch, A. Sadhanala, D. Harkin, J. Charmet, M. Hurhangee, A. Brown, S. Illig, P. Too, J. Jongman, I. McCulloch, J.-L. Bredas, H. Sirringhaus, *Nat. Mater.* **2017**, *16*, 356.
[28] L. Qiu, X. Wang, W. H. Lee, J. A. Lim, J. S. Kim, D. Kwak, K. Cho, *Chem. Mater.* **2009**, *21*, 4380.
[29] Y. Lei, P. Deng, J. Li, M. Lin, F. Zhu, T.-W. Ng, C.-S. Lee, B. S. Ong, *Sci. Rep.* **2016**, *6*, 24476.
[30] Z. He, Z. Zhang, S. Bi, *Mater. Adv.* **2022**, *3*, 1953.
[31] S. Goffri, C. Müller, N. Stingelin-Stutzmann, D. W. Breiby, C. P. Radano, J. W. Andreasen, R. Thompson, R. A. J. Janssen, M. M. Nielsen, P. Smith, H. Sirringhaus, *Nat. Mater.* **2006**, *5*, 950.
[32] Y.-Q. Zheng, Y. Liu, D. Zhong, S. Nikzad, S. Liu, Z. Yu, D. Liu, H.-C. Wu, C. Zhu, J. Li, H. Tran, J. B.-H. Tok, Z. Bao, *Science* **2021**, *373*, 88.
[33] Y. Lee, J. Y. Oh, W. Xu, O. Kim, T. R. Kim, J. Kang, Y. Kim, D. Son, J. B.-H. Tok, M. J. Park, Z. Bao, T.-W. Lee, *Sci. Adv.* **2018**, *4*, eaat7387.
[34] W. Niu, H.-C. Wu, J. R. Matthews, A. Tandia, Y. Li, A. L. Wallace, J. Kim, H. Wang, X. Li, K. Mehrotra, Z. Bao, M. He, *Macromolecules* **2018**, *51*, 9422.
[35] Z. Wang, Z. Liu, L. Ning, M. Xiao, Y. Yi, Z. Cai, A. Sadhanala, G. Zhang, W. Chen, H. Sirringhaus, D. Zhang, *Chem. Mater.* **2018**, *30*, 3090.
[36] L. Qiu, W. H. Lee, X. Wang, J. S. Kim, J. A. Lim, D. Kwak, S. Lee, K. Cho, *Adv. Mater.* **2009**, *21*, 1349.
[37] Q.-Y. Li, Z.-F. Yao, J.-Y. Wang, J. Pei, *Rep. Prog. Phys.* **2021**, *84*, 076601.
[38] H. Yang, G. Zhang, J. Zhu, W. He, S. Lan, L. Liao, H. Chen, T. Guo, *J. Phys. Chem. C* **2016**, *120*, 17282.
[39] W. H. Lee, Y. D. Park, *Polymers* **2014**, *6*, 1057.
[40] L. J. Richter, D. M. DeLongchamp, A. Amassian, *Chem. Rev.* **2017**, *117*, 6332.
[41] Y. Ito, A. A. Virkar, S. Mannsfeld, J. H. Oh, M. Toney, J. Locklin, Z. Bao, *J. Am. Chem. Soc.* **2009**, *131*, 9396.
[42] M. Kirkus, L. Wang, S. Mothy, D. Beljonne, J. Cornil, R. A. J. Janssen, S. C. J. Meskers, *J. Phys. Chem. A* **2012**, *116*, 7927.
[43] F. C. Spano, *Acc. Chem. Res.* **2010**, *43*, 429.
[44] S. Wood, J. Wade, M. Shahid, E. Collado-Fregoso, C. Bradley, D. D. C. , J. R. Durrant, M. Heeney, J.-S. Kim, *Energy Environ. Sci.* **2015**, *8*, 3222.
[45] Y.-J. Kim, N.-K. Kim, W.-T. Park, C. Liu, Y.-Y. Noh, D.-Y. Kim, *Adv. Funct. Mater.* **2019**, *29*, 1807786.
[46] D. T. Duong, V. Ho, Z. Shang, S. Mollinger, S. C. B. Mannsfeld, J. Dacuna, M. F. Toney, R. Segalman, A. Salleo, *Adv. Funct. Mater.* **2014**, *24*, 4515.
[47] J. Y. Na, B. Kang, Y. D. Park, *J. Phys. Chem. C* **2019**, *123*, 17102.
[48] J. Rivnay, S. C. B. Mannsfeld, C. E. Miller, A. Salleo, M. F. Toney, *Chem. Rev.* **2012**, *112*, 5488.
[49] D. Choi, M. Chang, E. Reichmanis, *Adv. Funct. Mater.* **2015**, *25*, 920.
[50] H. Tran, V. R. Feig, K. Liu, H.-C. Wu, R. Chen, J. Xu, K. Deisseroth, Z. Bao, *ACS Cent. Sci.* **2019**, *5*, 1884.
[51] A. Dazzi, C. B. Prater, *Chem. Rev.* **2017**, *117*, 5146.
[52] K. Xu, W. Sun, Y. Shao, F. Wei, X. Zhang, W. Wang, P. Li, *Nanotechnol. Rev.* **2018**, *7*, 605.
[53] K. Zhao, O. Wodo, D. Ren, H. U. Khan, M. R. Niazi, H. Hu, M. Abdelsamie, R. Li, E.r. Q. Li, L. Yu, B. Yan, M. M. Payne, J. Smith, J. E. Anthony, T. D. Anthopoulos, S. T. Thoroddsen, B. Ganapathysubramanian, *Adv. Funct. Mater.* **2016**, *26*, 1737.
[54] D. Natali, M. Caironi, *Adv. Mater.* **2012**, *24*, 1357.
[55] D. K. Owens, R. C. Wendt, *J. Appl. Polym. Sci.* **1969**, *13*, 1741.
[56] S. Pang, R. Zhang, C. Duan, S. Zhang, X. Gu, X. Liu, F. Huang, Y. Cao, *Adv. Energy Mater.* **2019**, *9*, 1901740.
[57] P. J. Flory, *Principles of Polymer Chemistry*, Cornell University Press, Ithaca, NY **1953**.
[58] M. M. Coleman, C. J. Serman, D. E. Bhagwagar, P. C. Painter, *Polymer* **1990**, *31*, 1187.
[59] D. J. Gundlach, J. E. Royer, S. K. Park, S. Subramanian, O. D. Jurchescu, B. H. Hamadani, A. J. Moad, R. J. Kline, L. C. Teague, O. Kirillov, C. A. Richter, J. G. Kushmerick, L. J. Richter, S. R. Parkin, T. N. Jackson, J. E. Anthony, *Nat. Mater.* **2008**, *7*, 216.